

Cone beam optical computed tomography for gel dosimetry I: scanner characterization

Tim Olding¹, Oliver Holmes¹ and L John Schreiner^{1,2}

¹ Department of Physics, Queen's University, Kingston, ON, K7L 3N6, Canada

² Cancer Centre of South Eastern Ontario at Kingston General Hospital, 25 King Street West, Kingston, ON, K7L 5P9, Canada

E-mail: tim.olding@krcc.on.ca

Received 13 November 2009, in final form 1 March 2010

Published 22 April 2010

Online at stacks.iop.org/PMB/55/2819

Abstract

The ongoing development of easily accessible, fast optical readout tools promises to remove one of the barriers to acceptance of gel dosimetry as a viable tool in cancer clinics. This paper describes the characterization of a number of basic properties of the VistaTM cone beam CCD-based optical scanner, which can obtain high resolution reconstructed data in less than 20 min total imaging and reconstruction time. The suitability of a filtered back projection cone beam reconstruction algorithm is established for optically absorbing dosimeters using this scanner configuration. The system was then shown to be capable of imaging an optically absorbing media-filled 1 L polyethylene terephthalate (PETE) jar dosimeter to a reconstructed voxel resolution of $0.5 \times 0.5 \times 0.5 \text{ mm}^3$. At this resolution, more than 60% of the imaged volume in the dosimeter exhibits minimal spatial distortion, a measurement accuracy of 3–4% and the mean to standard deviation signal-to-noise ratio greater than 100 over an optical absorption range of $0.06\text{--}0.18 \text{ cm}^{-1}$. An inter-day scan precision of 1% was demonstrated near the upper end of this range. Absorption measurements show evidence of stray light perturbation causing artifacts in the data, which if better managed would improve the accuracy of optical readout. Cone beam optical attenuation measurements of scattering dosimeters, on the other hand, are nonlinearly affected by angled scatter stray light. Scatter perturbation leads to significant cupping artifacts and other inaccuracies that greatly limit the readout of scattering polymer gel dosimeters with cone beam optical CT.

1. Introduction

Modern radiation therapy has been a rapidly evolving field over the last few decades, involving increasingly sophisticated treatment planning and delivery options toward the goal of delivering a sufficient and uniform dose to a target volume while sparing the surrounding healthy tissue,

in as short a treatment time frame as possible. While conventional one- and two-dimensional (1D, 2D) dosimetry tools such as ion chambers, diodes, arrays of ion chambers or diodes, film, etc available in the clinic are well suited to the task of regular quality assurance, there are particular circumstances (e.g. when bringing a new treatment on-line, or verifying small field deliveries) where a fully three-dimensional (3D) dosimetry tool would be a useful addition to the task of spatial dose verification of these sophisticated delivery options (Schreiner 2009).

Since the early development of gel dosimetry (Gore *et al* 1984, Olsson *et al* 1990), it has been recognized as a potential high resolution, tissue equivalent, 3D dosimeter for clinical use, but a number of factors have limited the uptake of this tool in the clinical environment (Schreiner and Olding 2009). One of the major limiting factors has been the lack of access to the first developed, and generally preferred gel dosimeter readout modality of magnetic resonance imaging (Gore *et al* 1984, Olsson *et al* 1990).

An alternative modality of optical readout was introduced in the mid-1990s (Tarte and van Doorn 1993, 1995, Gore *et al* 1996) which employed a He–Ne laser beam light source–photodiode detector pair in a translate–rotate scan path to acquire a set of transmitted light intensity projections through an irradiated cylindrical polymer gel dosimeter (Maryanski *et al* 1993, 1996) at different angles over 360°. Optical computed tomography (CT) techniques were then applied to obtain a reconstructed 3D optical attenuation map of the gel which could be calibrated against absorbed dose. The initial results from this system were exciting both in terms of measurement accuracy (better than 5%) and spatial resolution (<2 mm voxels).

The long scan time associated with the first-generation translate–rotate scanner in order to obtain a high resolution 3D data set has spurred the development of faster optical scanners, from improved translate–rotate scanners (van Doorn *et al* 2005, Lopatiuk-Tirpak *et al* 2008), to cone beam (Wolodzko *et al* 1999, Babic *et al* 2008) and parallel beam (Doran *et al* 2001, Krstajic and Doran 2006, 2007) charge-coupled device (CCD)-based configurations. While point detection laser–photodiode-based systems acquire point-by-point data, digital CCD detectors obtain a complete 2D area intensity transmission projection at a time. This introduces a tradeoff between the two systems. At present, point detection schemes can easily incorporate a collimator that rejects stray light from sources not along the primary ray path between the light source and the detector (Oldham and Kim 2004), but they may have scan times on the order of hours. CCD-based area detection schemes cannot easily incorporate physical collimation at the detector end of the scanner, and hence they accept stray light into the ray bundle passing through the lens aperture(s) and falling on the CCD detector, but can have a total scan time of less than 10 min. This fast scan time is particularly advantageous with the use of Fricke-based gel dosimeters, which exhibit a degradation of spatial integrity of dose information over time through diffusion of iron or chelated iron–dye complex ions (Olsson *et al* 1992, Kelly *et al* 1998).

Important work has been completed on the characterization of the parallel beam CCD scanner (Krstajic and Doran 2006, 2007), and there have been several studies of different translate–rotate scanners, for example, the investigations by Oldham *et al* (Oldham *et al* 2001, 2003, Oldham and Kim 2004) and Islam *et al* (2003). Some literature also exists on cone beam CCD scanners, primarily describing the commercial VISTA™ cone beam optical CT unit available from Modus Medical Devices Inc. (London, ON, Canada) (Wolodzko *et al* 1999, DeJean *et al* 2006a, 2006b, Jordan and Battista 2006a, 2006b, Bosi *et al* 2007, 2009). The cone beam system has the advantages of being low cost, compact and easily scalable, but early results indicate that this readout modality in particular is prone to scatter perturbation (Doran and Krstajic 2006).

This paper presents an investigation of the performance capabilities and limitations of the Vista cone beam optical CT scanner for use in the field of gel dosimetry. Results are reported

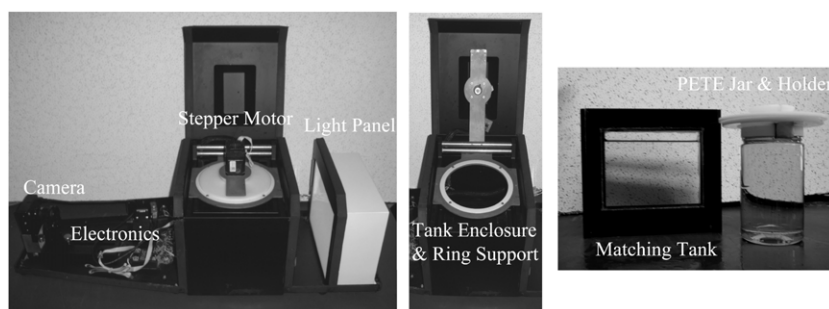


Figure 1. The Vista™ cone beam optical CT scanner used for volumetric imaging. This scanner contains a CCD camera with a 6.4° half cone imaging angle, a precision stepper motor for rotating the dosimeter jar, a dosimeter matching tank and an acrylic sheet-diffused light LED area light panel providing illumination at wavelengths of 590 nm and 633 nm. Custom 1 L PETE jars are suspended on the ring support in the matching tank sitting in the tank enclosure.

to provide a basic understanding of the effect of camera lens aperture selection, to validate the assertion of cone beam optical CT imaging geometry and to experimentally establish the high spatial resolution optical CT image reconstruction. The effects of geometric distortion in cone beam optical CT are then examined and the scanner measurement capabilities assessed through volume imaging of optically scattering and absorbing media in standard-sized 1 L polyethylene terephthalate (PETE) jars. These measurements were quantified over a range of mean optical scatter and absorption attenuation values in terms of attenuation linearity, accuracy, mean to standard deviation signal-to-noise ratio (SNR) and inter-day scan precision. While this work is particularly directed toward optical cone beam imaging of standard-sized 1 L PETE dosimeter jars, the results could be applied to other container sizes. The investigation presented in this paper is distinguished from previous reports (describing some of the basic properties listed above) by its broad scope of evaluation using a standard-sized gel dosimeter container and its justification of some of the basic assumptions fundamental to the use of cone beam optical CT.

2. Experiment

2.1. Cone beam optical CT imaging

The basic details of the optical CT imaging performed in this study and the preparation of scanner calibration solutions are outlined in this section. A Vista™ cone beam optical CT scanner (figure 1) was used for volume imaging, with either 633 or 590 nm LED diffuse light panel illumination (specified in each experiment) filtered by an optical band pass filter placed in front of the camera. Calibration parameters for the geometry shown in figure 2 (H_F , H_R , W_F , W_R , L and D_{SA}) were determined or calculated to be better than ± 0.5 mm using a metric ruler and a printed transparency checkerboard line grid, with 1 cm spacing between lines, inserted at the front and rear of the matching tank.

The normal practice was to let the scanner warm up for at least 1 h prior to performing a scan. For each scan, a set of 410 light intensity transmission projections was acquired over 360° to ensure adequate sampling in Fourier space during image reconstruction (Robb 1982, Guan and Gordon 1996). A 1024×768 pixel, 12-bit CCD camera (Dragonfly2 DR2-HIBW, Point Grey Research, Richmond, BC, Canada) using a $2/3''$ diameter, 12 mm focal length

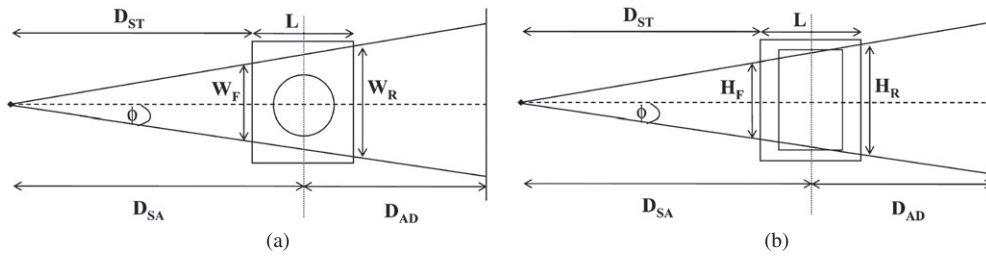


Figure 2. (a) Top and (b) side views of the Vista cone beam optical CT scanner geometry (adapted from the VistaRecon manual produced by Modus Medical Devices, Inc.).

lens (Computar M-1214-MP, Commack, NY, USA) set to an aperture setting of f5 (unless otherwise stated) was used in the scanner. Reference scans were completed on a 1 L PETE jar containing the matching tank solution held by a custom holder in the ring support, at the highest shutter exposure time possible (without inducing camera pixel saturation) and the lowest gain setting. Data scans were acquired at the same camera settings as the reference scan on the absorbing solutions, scattering solutions and gelatin phantoms. Reconstructed 3D linear optical attenuation data sets were obtained using the natural logarithmic ratio of the data and reference scans (note that a dark field image is acquired and subtracted from each scan) through use of the VistaRecon software. A Feldkamp filtered back-projection reconstruction algorithm with a Hamming filter (Feldkamp *et al* 1984) was used in the image reconstruction. A standard 4×4 pixel binning routine was applied to the projection data by the software for reconstruction to a 0.5 mm cubic voxel resolution, while 8×8 pixel binning was employed for a 1.0 mm cubic voxel resolution. The default resolution for scanner characterization data was 0.5 mm, unless otherwise specified.

The matching tank solution for the scanner consisted of 10–12 wt% propylene glycol–water mixtures, the refractive index (RI) of which was monitored over time at room temperature (21 ± 1 °C) using a handheld refractometer with a central measurement wavelength of 589 nm (r^2 mini refractometer, Reichert Analytical Instruments, Depew, NY, USA). Temperature measurements were taken using a digital temperature probe (TM99A-NA Digital Thermometer, Nuclear Associates, Carle Place, NY, USA).

Note that one of the primary goals for using a cone beam charge-coupled device (CCD)-based configuration is to improve the scan time over that of the point-detection schemes. For an aperture setting of f5 and a maximum shutter speed of 133.2 ms (gain set to zero) under 590 nm illumination, reference and data scans are acquired in just over 4 min each, and a $12.8 \times 12.8 \times 12.8$ cm³ sized volume image of a 0.5 mm cubic voxel size resolution is reconstructed in 10 min, using a standard desktop computer. The hardware and software configurations for this total imaging time less than 20 min are not optimized. While it is outside the scope of this paper, further imaging time reduction is certainly achievable.

To test the performance of the cone beam scanner under scattering conditions, scattering solutions and gelatin phantoms were employed that allowed the characterization of the range of optical measurement integrity and accompanying performance limitations of the scanner to be separated from the uncertainties in dose delivery and gel dosimetry. Previous studies employing calibration scattering solutions and phantoms for optical CT scanner characterization (Bosi *et al* 2007, 2009) have involved the use of a turbid colloidal suspension of Dettol™ antiseptic (Reckitt Benckiser, West Ryde, Australia) in water–gelatin mixtures. In this work, an alternative acrylic latex scattering emulsion (Duramax B-1000, Rohm & Haas) was identified for use. This scattering emulsion can be diluted by water, and maintains

uniformity and stability of colloidal distribution in heated, refrigerated and room temperature formulations of water, propylene glycol and gelatin. These features were important for the preparation of scattering solutions and gel phantoms that mimic the scattering and refractive index properties of typical Fricke–xyleneol and polymer gel-based dosimeter recipes. The Duramax-based solution is similar in performance to the Dettol-based solution prepared by Bosi *et al* but was preferred as (1) the solution comes pre-formulated as an emulsion and only requires a simple dilution step to achieve different concentrations with high accuracy, (2) the particle size distribution does not vary during preparation, whereas Dettol produces a variable particle size distribution each time it is mixed with water and (3) acrylic has a similar refractive index to the acrylamide monomer commonly used in polymer gel dosimetry.

Calibration scattering solutions were prepared through addition of small amounts of Duramax B-1000 to mixtures of 12 wt% propylene glycol (Cat. No. 134 368, Sigma-Aldrich Ltd, Oakville, Canada) in water. These solutions were then poured into 1 L PETE containers and stored at room temperature prior to optical measurement. A diluted sample of the Duramax B-1000 acrylic latex emulsion was independently assessed using a Fritsch particle sizer (Fritsch GmbH, Germany) and the particle size distribution determined to have a mean particle size of $370 \pm 140 \mu\text{m}$, which is on the same order as the size of polymerized particles in polymer gel dosimeters (Maryanski *et al* 1996, Oldham *et al* 2003). The refractive index of the calibration scattering solutions was verified at room temperature ($21 \pm 1 \text{ }^\circ\text{C}$) using the n^2 mini refractometer over a period of 16 months and found to be consistent within a measurement uncertainty of ± 0.001 .

A gelatin phantom was prepared by adding 5 wt% gelatin (300 bloom Type A porcine gelatin, Cat. No. G2500, Sigma-Aldrich Ltd, Oakville, Canada) to room temperature distilled, de-ionized water. The mixture was allowed to swell for 15 min, and then heated to $45 \text{ }^\circ\text{C}$ for 5 min to dissolve the gelatin. The heated solution was poured into a 1 L PETE container and placed in the refrigerator overnight to set the gelatin. The gelatin-filled container was brought to room temperature conditions prior to optical scanning.

To test the performance of the cone beam scanner under absorbing conditions, calibration absorbing solutions were prepared by adding small amounts of patent blue violet dye (Cat. No. 198 218, Sigma-Aldrich Ltd, Oakville, Canada) to mixtures of 12 wt% propylene glycol in water, poured into 1 L PETE containers and stored at room temperature prior to optical scanning.

Line profiles and regions of interest (ROI) in absorbing, scattering and gelatin phantom projection data and optical CT reconstructed 3D data sets were evaluated using the ImageJ (National Institute of Health, Bethesda, MD, USA), Microview 2.1.2 (GE Healthcare, UK) or MatLab (Mathworks, Newark, NJ) software.

2.2. Cone beam geometry validation

The first step in acquiring a basic understanding of cone beam optical imaging is to validate the geometry under optically absorbing conditions. The typical scenario in x-ray cone beam computed tomography (CBCT) involves the measurement of the x-rays along ray paths projected in a 3D solid angle from a point source (Kak and Slaney 1998). Optical CT imaging with a cone beam optical scanner, on the other hand, employs projection images acquired using a digital camera with a finite detector area from diffuse light source illumination through a 3D semi-transparent (or attenuating) volume. The validity of the cone beam reconstruction algorithm in this scenario is therefore not inherently obvious. Referring to figure 3 (which is not drawn to scale for purpose of illustration), there is a small ray bundle of light centered on each primary ray path from the diffuse light source to the CCD detector chip that is actually

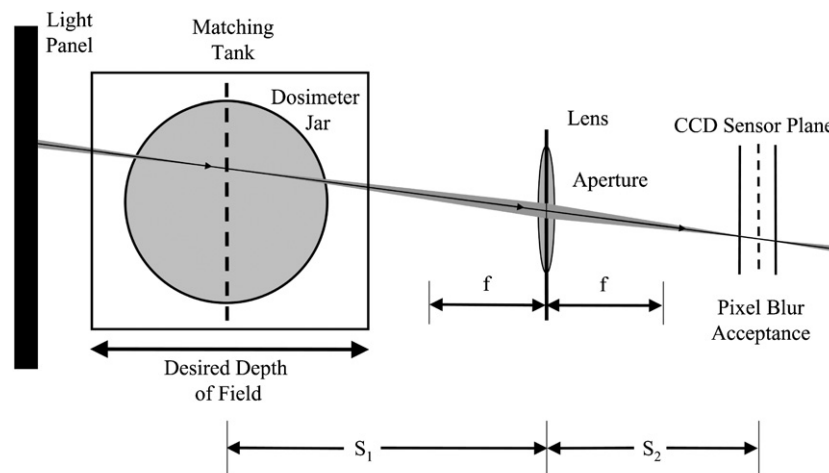


Figure 3. Illustration of the imaging optics for the cone beam CCD-based configuration (not to scale).

focused through the camera lens onto each CCD pixel. The size of this ray bundle (the edges of which are termed ‘marginal’ rays) is affected by the properties of the lens such as focal length, aperture settings within the lens (i.e. the f-stop), the distances between the light source, imaging volume and detector, the depth of field, etc. In the ideal scenario, the signal acquired at each detector pixel would come from light attenuated along a single cone beam geometry ray path through the object space. However, while the acceptance of a single ray path at each detector pixel is not a practical reality, the lens-based camera approximately adheres to the cone beam geometry by only focusing light that has traveled in a tight ray bundle along cone beam primary ray path geometry to the CCD detector. This approximation becomes less valid as the ‘angle of acceptance’ of light reaching each point (or pixel) in the detector array increases. That is, individual ray bundles can be thought of as occupying a volume ‘light cone’ with the base of the cone at the light source and vertex ‘angle of acceptance’ at the corresponding detector pixel. The approximation to cone beam geometry can be given a mathematical description (Marks *et al* 2001), and depends on the camera settings being optimized toward a small acceptance angle light cone, such that the base of the cone decreases toward a point source of light and the volume of the cone toward encompassing a single cone beam ray path.

The thin lens law states that a given object plane will be in focus at the CCD sensor plane when $(S_1)^{-1} + (S_2)^{-1} = f^{-1}$, where $S_1, S_2 \geq f$. For a given pixel area and camera lens setting, there is a detector-to-object distance range for which points on the cone beam primary ray path through the object space in that range will focus to a finite sized point ‘blur’ accepted to the area of a single pixel on the CCD sensor image plane, a range that is termed the depth of field. Outside that range, points on the primary ray path will be imaged as a blurred circle on the image plane, termed the ‘circle of confusion’. Therefore, it is important to maintain a depth of field that covers the entire imaged volume to satisfy the cone beam geometry, otherwise the image acquired by the camera will be blurred, and hence there will be a degradation of spatial information. For a given source–detector geometry and camera lens, the f-stop setting influences several variables. High f-stops can result in diffraction-related aberrations and low f-stops may allow spherical aberrations from the lens to affect the projection image (for

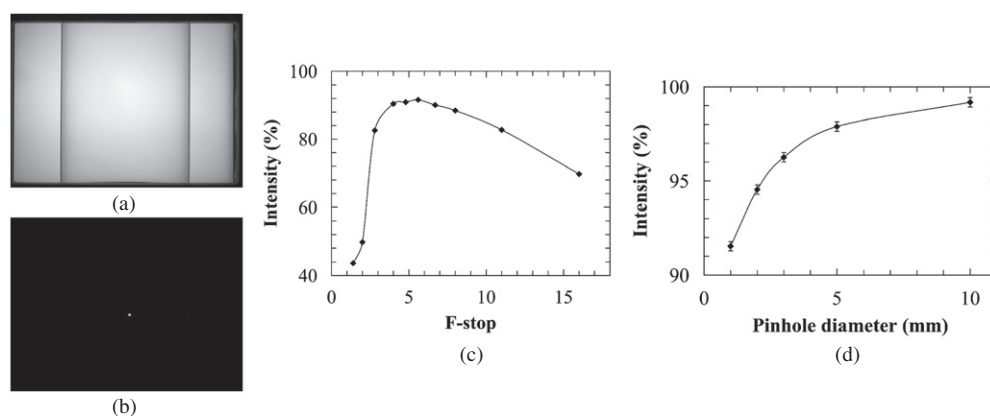


Figure 4. (a) Open field and (b) 1 mm pinhole blocker projection images from the Vista scanner with a 1 L PETE jar in the matching tank. Pinhole blocker ‘center pixel’ intensity is extracted from the ‘blocked’ projection image and expressed as a percentage of open field intensity at the same pixel from the open field projection image for: (c) a 1 mm diameter pinhole at varied camera aperture, and (d) for varied diameter single pinholes at f5 with the single pinhole beam pass insert placed at the light source side of the matching tank. Lines are included to aid the eye. Some of the error bars are smaller than symbol size.

example, see Hillier (1949)). Raising the f-stop narrows the ray bundle (or light cone angle of acceptance), but also reduces the collection efficiency of the lens. This necessitates an increased shutter time and raised camera gain, which can increase scan time and noise level respectively of the scan measurements. To investigate the balance of these parameters further and verify the assertion of cone beam geometry, some basic experiments were performed on the Vista scanner.

The effect of camera lens aperture (f-stop) setting on cone beam geometry was investigated through analysis of transmission projection images taken at 590 nm of a 1 L PETE jar containing the 12 wt% propylene glycol–water matching tank solution. Images were acquired over the range of camera lens f-stops under open field illumination (figure 4(a)) and with a single 1 mm diameter pinhole blocker (machined in a 1/32" matte-coated aluminum sheet) inserted at the light source side of the matching tank (figure 4(b)). The peak ‘center pixel’ intensity with the pinhole blocker in place (i.e. the intensity value at the center pixel in the circular area of illuminated detector pixels) was compared to the light intensity recorded at the same ‘center pixel’ location under open field illumination. The percentage of center pixel pinhole-to-open-field intensity reaches a maximum value above 90% over a relatively broad f-stop range of f4–f6.7 (figure 4(c)).

Figure 4(d) shows results from a second set of transmission projection images taken at 590 nm of a 1 L PETE jar containing the same 12 wt% propylene glycol–water solution as used in the Vista scanner. In this experiment, images were acquired under open field illumination and for single pinhole blockers of varying diameter inserted at the light source side of the matching tank at an f-stop of f5. The center pixel intensity through the pinhole blocker for pinhole diameters in the range of 1–10 mm ranged from approximately 91% to 99%+ of the value for the same pixel under open field illumination. That is, over 99% of the light received at the detector pixel falls within a light cone volume described by a cone vertex angle of $\sim 0.9^\circ$ at the detector pixel and 10 mm diameter base at the light source, and approximately 90% of that light originates from an even more restricted vertex angle of $\sim 0.1^\circ$, as calculated using the pinhole diameter and the pinhole blocker-to-detector distance of 66.0 ± 0.1 cm.

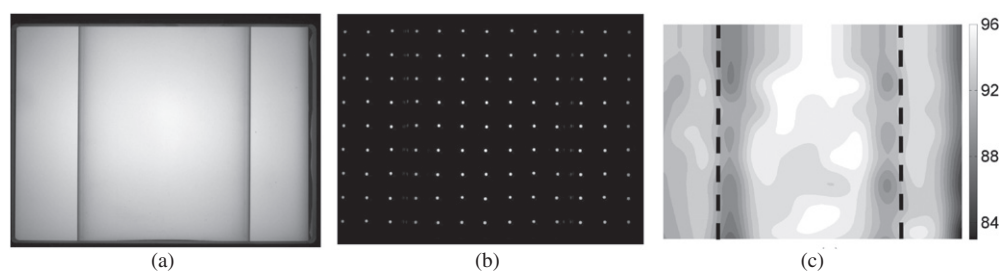


Figure 5. (a) Open field and (b) pinhole grid projection images from the Vista scanner with a 1 L PETE jar in the matching tank. Each pinhole blocker ‘center pixel’ intensity is extracted from the ‘blocked’ projection image and expressed as a percentage of open field intensity at the same pixel from the open field projection image. These values were used to calculate (c) an interpolated percentage map over the full 2D region. The dashed lines show the approximate location of the jar edges from the projection data.

The results in figure 4 were extended to two dimensions by using the same scanner setup and replacing the single pinhole blocker with a pinhole grid blocker machined with 2 mm diameter pinholes spaced 11 mm apart in the 1/32" matte-coated aluminum sheet and inserted at the light source side of the matching tank. The objective of the pinhole grid blocker experiment was to validate the cone beam geometry at regularly spaced points over the full two-dimensional area of the projection at the chosen f -stop of $f5$. This blocker grid (or beam pass array) approach has previously been used in the evaluation of optical CT projection images (Olding *et al* 2009, Jordan and Battista 2009a), but has been extended to a full two-dimensional analysis in this work. Open field (figure 5(a)) and pinhole grid projection images (figure 5(b)) were acquired, and each pinhole ‘center pixel’ intensity was extracted from the ‘blocked’ projection image and expressed as a percentage of open field intensity at the same pixel from the open field projection image. A bi-cubic spline function in Matlab was used to interpolate between measured grid points to obtain a 2D percentage map for the full projection image (figure 5(c)). The reported values in the map then indicate how much of the light intensity recorded at each pixel in the detector travels in the ‘tight ray bundle’ or light cone volume that is centered on the primary cone beam ray path, and defined by the 2 mm diameter pinhole opening and the pinhole blocker-to-detector distance of 66.0 ± 0.1 cm. Hence, this percentage map represents a measure of adherence to cone beam geometry across the full 2D projection image. The 2 mm grid measurement was then repeated, replacing the jar containing matching tank solution with two jars containing a 12 wt% propylene-glycol mixture and 0.74 mg L^{-1} and 1.48 mg L^{-1} of patent blue violet absorbing dye, respectively. Percentage maps were obtained as before and found to be approximately equivalent to that obtained for the matching tank fluid-filled jar.

2.3. Spatial resolution

The ability of an imaging system to distinguish between two closely spaced objects (i.e. the spatial resolution of the scanner) can be described by the modulation transfer function (MTF), which is a measure of spatial frequency response in terms of contrast at a given spatial frequency relative to a well-defined low frequency. Reconstructed optical CT image MTFs have previously been evaluated for a laser-based and a parallel-beam CCD scanner using the wire method (Oldham and Kim 2004, Doran *et al* 2004). In their investigations, a thin wire was scanned and the line spread function of the reconstructed CT image was determined,

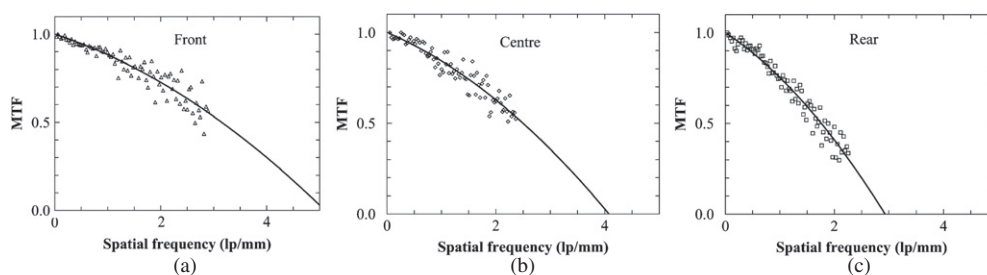


Figure 6. Modulation transfer function of the projection data obtained from imaging a sinusoidal test pattern on the 2003 Koren lens test chart (www.normankoren.com) located along the central axis at the (a) front, (b) center and (c) rear of the Vista scanner matching tank, referenced against the camera position. The MTF for each data set was fit with a third-order polynomial to aid the eye. Error bars are smaller than the symbol size.

with a de-convolution correction accounting for the finite wire diameter. In-depth studies evaluating the MTF of the actual (irradiated) polymer gel with an MRI system have also been completed (Berg *et al* 2004, Bayreder *et al* 2008). Projection MTFs have also been obtained for the parallel beam CCD system using a high quality test target with an MTF sinusoidal test pattern (from Edmund Optics) located at different detector–target distances (Krstajic and Doran 2007).

In order to establish the spatial resolution and depth of field of the Vista scanner, an imaging test target (the 2003 Koren lens test chart) similar to the high quality test target used by Krstajic and Doran (2007) was obtained from www.normankoren.com. Projection images were taken at 590 nm with the test target positioned in the matching tank fluid along the optical axis at the front, center and rear of the matching tank (camera-to-target distances of 49.9 ± 0.1 cm, 57.5 ± 0.1 cm and 65.1 ± 0.1 cm, respectively). Projection MTFs were then derived from the sinusoidal MTF test pattern data in the image (figure 6). A projection image and calculated MTF were also obtained for the test target inserted at the rear of the tank as before, but with a 1 L PETE jar containing a 5 wt% gelatin–water mixture inserted in the matching bath. In this case, the MTF decreased to 50% at a spacing of approximately 1.6 line pairs mm^{-1} . This is slightly more than a 10% reduction in projection image resolution from the previous experiment, which showed the MTF decreasing to 50% at approximately 1.8 line pairs mm^{-1} (at the rear of the tank, see figure 6(c)).

The scatter in the measured data reported in figure 6 can partially be attributed to the print quality of the test target.

The depth of field criterion for satisfying the cone beam geometry condition (Kak and Slaney 1988) of the scanner was set to be the axial range (distance from the detector to the object plane) over which the image contrast of a square wave pattern at 2 line pairs mm^{-1} on the 2003 Koren lens test chart was 50% of the maximum imaged contrast at the lowest frequency line spacing on the test chart. The necessary data were acquired by imaging the test target at 590 nm over a range of f-stops in the matching tank fluid at the front and rear of the tank. An MTF of 50% (or more) at 2 line pairs mm^{-1} was obtained from the square wave pattern image data for f-stops of f4 or greater.

2.4. Spatial distortion

The effect of index of refraction mismatch on geometric distortion of optical CT reconstructed images was investigated through use of a custom in-house built pin phantom. The phantom consisted of a spiral pattern of stainless steel pins supported by an acrylic frame similar in

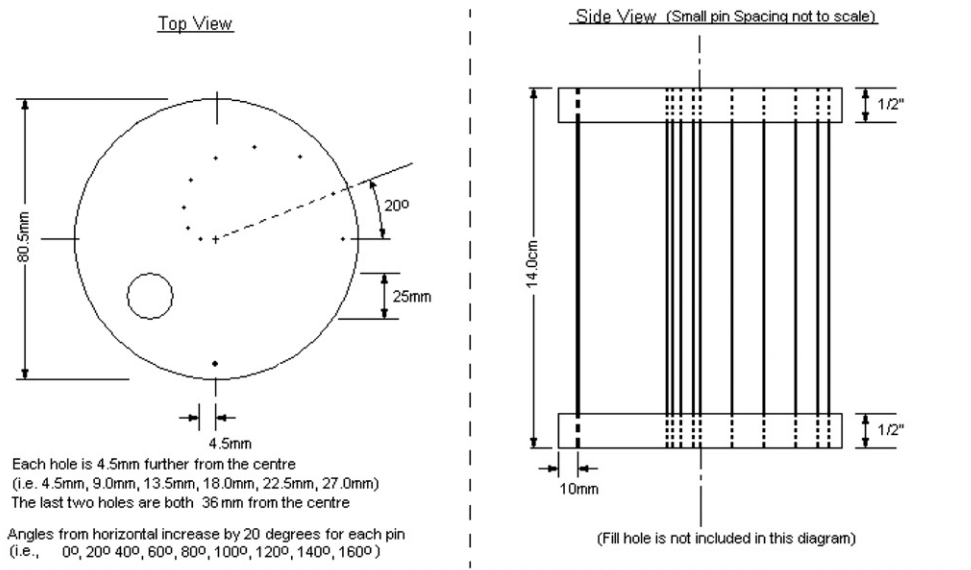


Figure 7. A pin phantom consisting of a series of stainless steel pins supported by an acrylic frame, designed to be inserted into a standard 1 L PETE dosimeter jar.

concept to the needle phantom employed by Oldham and Kim (2004), but designed to be inserted into a standard 1 L PETE dosimeter jar (see figure 7). In this way, the index of refraction, scattering and absorbing properties of the media within the jar could be easily adjusted, to explore their individual effects on the imaging of pin positions.

Two different matching tank solution formulations based on propylene glycol and glycerol were investigated. Both of these chemicals have previously been used for index matching, depending on the dosimeter being imaged. Glycerol has the advantage of a wider refractive index range for imaging high refractive index dosimeters, while propylene glycol is generally preferred, as it is not degraded by biological activity over time. For the propylene glycol trial, the tank media was kept at 10 wt% propylene glycol in water, corresponding to an optical index of refraction of 1.344 ± 0.001 at 21 °C, while the jar concentration was adjusted from 0–12 wt% propylene glycol in water. A 3D image of the pin phantom was reconstructed from optical CT measurements for each concentration. Similar measurements were performed for the glycerol trial, with the exception that the range of jar concentrations corresponded to 0–20% wt% glycerol. The concentration of the tank media for the glycerol trial was 19.4 wt% in water, corresponding to an optical index of refraction of 1.356 ± 0.001 at 21°C. Measurements were acquired for the distance between the central pin positioned at the scanner axis of rotation and each of the other eight pins in the phantom using: (1) the optical CT volume image data and (2) vernier calipers, which are considered to be accurate to ± 0.1 mm. The percentage radial compression was then calculated from the ratio of optical CT-measured distance to vernier caliper-measured distance for each of the eight pin separations for each slice in the optical CT data set, obtaining an average percentage radial compression for each pin (a total of 800 measurements in the optical CT image volume) relative to the ‘true’ vernier caliper measurement.

Matching the bath and jar media refractive indices reduces reconstructed image blurring, as seen through a visual comparison of the reconstructed image slices shown in figures 8(a)

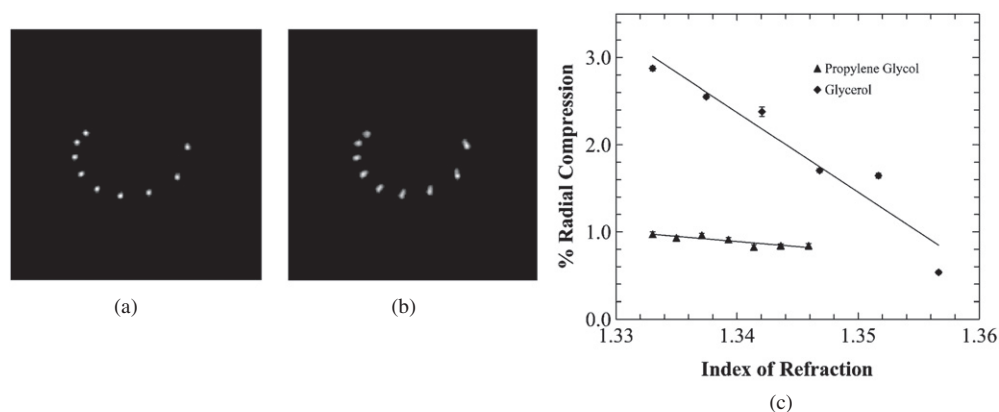


Figure 8. (a), (b) 2D slices of 3D optical CT images of the pin phantom. One image (b) exhibits the case of mismatch in index, while the other (a) shows the matching case. (c) Mean radial compression of pin positions in cone beam optical CT measurements at various jar concentrations of propylene glycol or glycerol and water. For most of the data points the errors bars are smaller than symbol size.

and (b). In the matched condition, the average radial compression under room temperature conditions was found to be $0.54 \pm 0.02\%$ for glycerol and $0.84 \pm 0.02\%$ for propylene glycol, corresponding to geometric distortions in the range of 0.2–0.3 mm. The average radial distortions for the full range of tank media concentrations are indicated in figure 8(c). The maximum radial compression observed in all trials was 4.5% at the third pin away from the center pin.

2.5. Scanner scatter measurement

The starting point for the assessment of scanner scatter measurement linearity was to acquire reference and data scan projection data sets of the matching tank containing the 12 wt% propylene glycol–water mixture in the Vista scanner at 633 nm. Three 8 cm diameter, 1 cm high cylindrical regions of interest (ROI) were evaluated at the top, middle and bottom of the reconstructed volume (figure 9(a)) and found to have values of $0.000 \pm 0.003 \text{ cm}^{-1}$, $0.0000 \pm 0.0005 \text{ cm}^{-1}$ and $0.000 \pm 0.001 \text{ cm}^{-1}$, respectively. A second projection data set was then acquired with 5 wt% gelatin in a water-filled 1 L PETE jar in the matching tank. Three 8 cm diameter, 1 cm high ROI centered in the PETE jar near the top, middle and bottom of the reconstructed volume were evaluated as before, and found to have mean attenuation values of $0.04 \pm 0.01 \text{ cm}^{-1}$, $0.044 \pm 0.001 \text{ cm}^{-1}$ and $0.045 \pm 0.006 \text{ cm}^{-1}$, respectively (figure 9(b)).

Most of the dosimeters used in gel dosimetry have a gelatin or agarose matrix used to spatially fix the dose data after irradiation. Hence, imaging a gelatin ‘blank’ can be thought of as the next step beyond imaging a PETE jar containing the matching tank solution. Profiles through the reconstructed optical CT image of the 5 wt% gelatin-in-water-filled 1 L PETE jar phantom (figure 9(c)) under 590 nm and 633 nm illuminations reveal additional data perturbation seen as cupping in the reconstructed data when the scattering media is introduced.

To further investigate the limitations imposed by cupping and other effects arising from the optical cone beam readout of scattering polymer gel dosimeters, a series of calibration scattering solutions in 1 L PETE jars were then imaged using the Vista scanner.

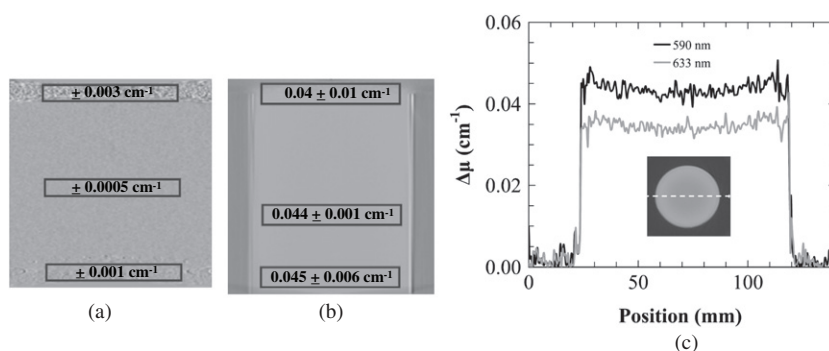


Figure 9. Reconstructed volume cross-sections showing standard deviation in mean attenuation for selected cylindrical regions of interest (ROI) in (a) the fluid-filled matching tank, with (b) a 5 wt% gelatin-in-water-filled 1 L PETE jar inserted in the fluid-filled tank. High uncertainty regions are observed at the top and bottom of the volume in both cases. The results in (c) show reconstructed attenuation profiles through a 5 wt% gelatin-in-water-filled 1 L PETE jar imaged at 590 nm and 633 nm.

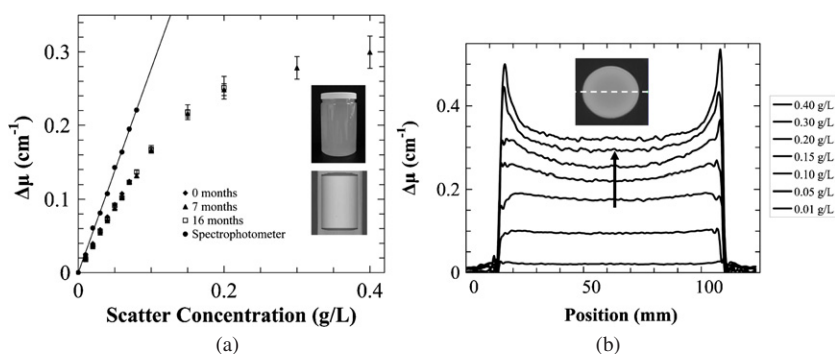


Figure 10. (a) Mean attenuation coefficients of uniform acrylic scattering solutions in 1 L PETE jars (top-right inset) from the Vista scanner, measured from an 8 cm diameter, 10 cm high cylindrical ROI in the image data (bottom-right inset) and spectrophotometer measurements using 10 mm PMMA cuvettes. A linear fit to the spectrophotometer data is shown in the plot. (b) Reconstructed (1.0 mm cubic voxel resolution) profiles across the scattering solutions (the arrow indicates the direction of increasing scatter concentration).

Small portions of the varied concentration scattering solutions were also separated into 10 mm polymethyl-methacrylate (PMMA) cuvettes and evaluated using an Ultrospec 1000 UV/visible spectrophotometer (Biochrom Ltd, Cambridge, UK). As the spectrophotometer provides better than 0.5–1.0% accuracy in transmission measurement, the spectrophotometer results were considered to be a reasonably ‘true’ assessment of calibration solution attenuation. Figure 10(a) shows that spectrophotometer-measured optical attenuation values obtained under room temperature conditions at 633 nm are linear with scatter concentration in the range of 0.01–0.08 g L⁻¹. The measurements showed reasonable long-term stability in mean optical attenuation coefficient and refractive index over 16 months of measurement. However, when the Vista scanner is used to image the full set of calibration scattering solutions in 1 L PETE jars (from which the 10 mm cuvettes were filled), the measured mean optical attenuation values in an 8 cm diameter, 10 cm high ROI centered in the jar volume image clearly depart in a nonlinear fashion from the corresponding spectrophotometer values over the full range

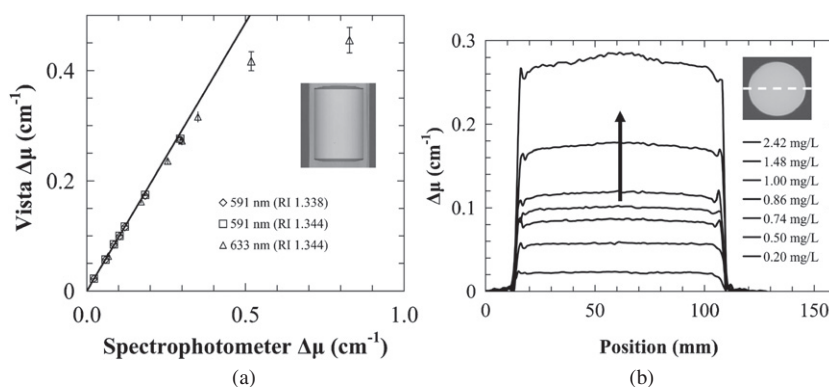


Figure 11. (a) Comparison of mean attenuation values (ROI as in figure 10) from 1 L PETE jars and 10 mm PMMA cuvettes filled with uniform absorbing dye solutions: (1) at two wavelengths and two different matching bath refractive indices (RI) using the cone beam Vista scanner and (2) at 590 nm and 633 nm using an UltroSpec 1000 UV-Vis spectrophotometer. A linear fit to the 590 nm (RI 1.344) data in the range of 0.0–0.2 cm^{-1} is shown in this plot. (b) Reconstructed (1.0 mm cubic voxel resolution) profiles across the uniform absorbing solutions imaged at 590 nm and a refractive index of 1.344 (the arrow indicates the direction of increasing dye concentration).

of jar scatter concentration (figure 10(a)). The variation in the mean ROI attenuation value between the three scan trials completed at different times in the 16 months' period ranged from 2 to 6% for the different concentrations. Figure 10(b) shows profiles across 1.0 mm cubic voxel resolution reconstructed optical CT volume images of the calibration scattering solutions, indicating an increase in cupping of the data with scatter concentration. The profiles are reconstructed at a lower voxel resolution than the data in figure 10(a) in order to observe underlying artifacts with reduced noise.

2.6. Scanner absorption measurement

While the dose contrast mechanism in polymer gel-based dosimeters is scattering of visible light, Fricke-based dosimeters contrast dose by light absorption. To investigate the performance of the Vista scanner under absorbing conditions, a series of calibration absorbing solutions in 1 L PETE jars were imaged using the Vista scanner. Small quantities of the varied concentration absorbing solutions were also separated into 10 mm PMMA cuvettes for spectrophotometer measurement, as before.

In contrast to the scattering solutions, the mean attenuation measurements of absorbing solutions from the Vista scanner (from the same ROI as in figure 10(a)) can be fit to a linear relationship against spectrophotometer measurement under both measurement wavelengths of 590 nm and 633 nm (figure 11(a)). The slope of the fit is slightly less than unity at 0.973 ± 0.004 (with an R^2 value of 0.9994) for the 590 nm (RI 1.344) data in the range of 0.0–0.2 cm^{-1} . A linear fit to the 590 nm (RI 1.338) data over the same attenuation range was found to have only a slightly lower slope at 0.967 ± 0.004 . The slope was not determined from the 633 nm data, as there were only two data points falling in the same 0.0–0.2 cm^{-1} attenuation range. At mean jar attenuations greater than roughly 0.2 cm^{-1} , the Vista measurement starts to depart from linearity. A bowing artifact is observed in the reconstructed profiles of the absorbing solutions (figure 11(b)); this becomes more pronounced at higher absorption values.

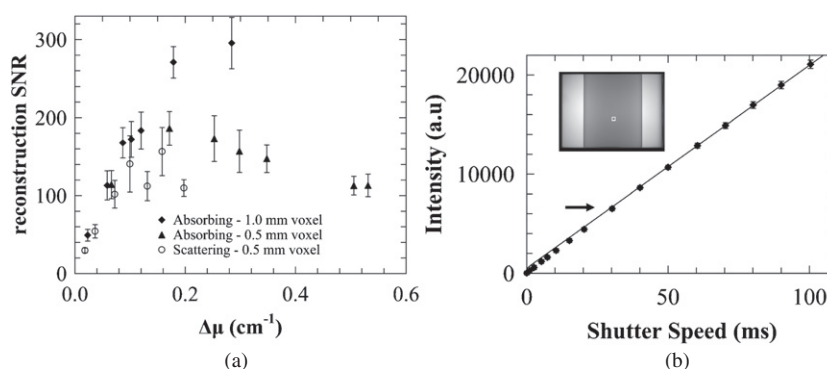


Figure 12. (a) Reconstructed mean to standard deviation signal-to-noise ratio for absorbing and scattering media-filled 1 L PETE jars imaged with the Vista scanner. Each data point represents the average of nine measurements from a $5 \times 5 \times 1$ voxel³ ROI located at different positions in the jar region of the optical CT image. (b) Camera pixel response linearity for a 20×20 pixel area in the projection image of a 0.74 mg L^{-1} absorbing solution. Some of the error bars are smaller than the symbol size. A linear fit to the data above 10 000 au is shown in the plot. The arrow indicates the approximate point of departure from linearity.

Table 1. Scanner measurement precision.

Scan no	Trial 1 mean attenuation (cm^{-1})	Trial 2 mean attenuation (cm^{-1})
1	0.1743 ± 0.0022	0.1730 ± 0.0022
2	0.1742 ± 0.0022	0.1727 ± 0.0023
3	0.1742 ± 0.0022	0.1728 ± 0.0023
4	0.1742 ± 0.0022	0.1728 ± 0.0022
5	0.1741 ± 0.0022	0.1729 ± 0.0022

Mean attenuation values are recorded in table 1 for a representative 25 mm diameter ROI slice centered on the jar axis in the reconstructed volume of a 1.48 mg L^{-1} absorbing solution. The recorded values are from five different scans acquired over a period of time spanning 6 h each on two separate days (designated trials 1 and 2) with careful attention to scanner warm-up time, as well as keeping the light source on throughout both scans and using the optional Vista software projection normalization region. Same day and inter-day measurement precisions better than 0.1% and 1.0% are indicated for this absorbing solution concentration/attenuation.

To determine the mean to standard deviation signal-to-noise ratio (SNR) for varied concentrations of scattering and absorbing media-filled 1 L PETE jars in the Vista scanner, a $5 \times 5 \times 1$ voxels³ (i.e. 25 voxels) SNR-ROI was set for evaluation of both image resolutions. Each data point shown in figure 12(a) represents the average of 9 SNR-ROI measurements at different positions in the jar region of the optical CT image (three positions at each of three heights within the cylindrical ROI used in figure 10(a)). The 0.5 mm cubic voxel resolution data were acquired under 633 nm illumination and the 1 mm cubic voxel resolution data under 590 nm illumination.

The mean transmitted intensity value within a 20×20 pixel area at a representative location in the projection image of a 0.74 mg L^{-1} absorbing solution (shown in figure 12(b)) was recorded over a range of camera shutter speeds under 590 nm illumination at f5

(figure 12(b)). A departure from linearity is observed at an intensity of ~ 6500 arbitrary units (au), which is approximately 10% of the camera full scale intensity (65 536 au).

3. Discussion

3.1. Cone beam geometry validation

The results of the single point measurements from the cone beam CT validation experiments (figure 4(c)) suggest that there is some flexibility in the choice of camera lens aperture (f-stop) to satisfy the cone beam geometry condition in the imaged object space of the Vista scanner. A relatively broad range of f-stops from f4 to f6.7 could be used. An f-stop of f5 was selected as the default setting for the scanner in all subsequent imaging. This f-stop was deemed to be a good compromise between reasonable light collection efficiency and an appropriate depth of field covering the entire matching tank measurement volume. A rapid fall-off in the ratio of center pixel pinhole-to-open-field intensity is observed for f-stops decreasing below f4, due to the fact that the depth of field does not fully cover the matching tank measurement volume, and moves outside the condition of cone beam geometry. Above f6.7, the ratio of center pixel pinhole-to-open-field intensity decreases more slowly, but the light collection efficiency of the CCD detector is very low, causing a significant decrease in the SNR (with a necessary increase in the camera gain).

The two-dimensional evaluation of the projection image area using the 2 mm pinhole grid blocker (figure 5(c)) shows that most of the jar region in the map reaches a value near 95%. Lower values are obtained near the jar edge due to the refractive index mismatch-driven re-direction of light at the matching fluid–jar wall interface. This is an unavoidable effect resulting from the use of PETE jars, which have an index of refraction of 1.575 at 590 nm. Raising the refractive index of the matching bath and gel dosimeter from the typical range of 1.34–1.36 at 590 nm and 21 °C to that of PETE material is not pragmatic, mainly due to the deleterious changes that would be required in the chemistry of the gel dosimeter in moving away from a primarily water-based formulation.

Despite this slight percentage variation within the jar region, the overall high percentage ratio of 95% indicates good conformation of the detected light to the preferred geometry within the ray path ‘light cone’ volume defined between the 2 mm diameter pinhole and each individual detector pixel. This indicates that the Vista scanner using 590 nm illumination reasonably satisfies the ‘narrow ray bundle’ cone beam geometry description for imaging of absorbing solutions, at least up to the value of $0.173 \pm 0.001 \text{ cm}^{-1}$ for the 1.48 mg L^{-1} patent blue violet dye solution.

3.2. Spatial resolution

The high resolution reconstruction capability of the Vista cone beam optical scanner has been, up to this point, assumed in the literature. The results shown in figure 6 now give a good basis for implementing the $0.5 \times 0.5 \times 0.5 \text{ mm}^3$ voxel size reconstruction of cone beam-imaged optically absorbing dosimeters, with a stringent requirement of a projection MTF value of 50% or greater at 2 line pairs mm^{-1} serving as the basis of this assessment (versus an MTF value of 10–20% or greater at 2 line pairs mm^{-1} discussed in other reports, for example, see Krstajic and Doran 2007). The standard PETE dosimeter jar has a diameter of $9.2 \pm 0.1 \text{ cm}$ and is held in position in the center of the tank during scanning. The lowest projection image resolution will be obtained at the rear of the jar (referenced in terms of distance away from the detector), which is located 4.6 cm along the 7.6 cm total distance from the center to the

rear of the tank. Also, the MTF value decreases to 50% at an approximate line spacing of 3.2 line pairs mm^{-1} at the front of the tank, 2.5 line pairs mm^{-1} at the center of the tank and 1.8 line pairs mm^{-1} at the rear of the tank (see figures 6(a)–(c)). Given that the line spacing resolution falls off approximately linearly with the distance from the front to the rear of the tank, the lowest resolution position in the PETE jar (i.e. at the rear of the jar) should then have an MTF value decreasing to 50% at approximately 2.1 line pairs mm^{-1} . This result satisfies the above criterion for imaging an optically absorbing media-filled PETE jar dosimeter positioned in the center of the matching tank to a 0.5 mm cubic voxel resolution (at least from analysis of transmission projection images). As most absorbing gel dosimeters also exhibit optical scattering due to the gel matrix component (e.g., gelatin or agarose) used to spatially fix the dose, further reduction in spatial resolution is expected from the ‘ideal’ absorbing case due to convolution of a scatter kernel onto the transmission data. The scattering MTF result for the 5 wt% gelatin-in-water phantom indicates a slight degradation in the spatial resolution that is consistent with this assertion. However, the results from the gelatin phantom experiment still indicate that a $0.5 \times 0.5 \times 0.5 \text{ mm}^3$ voxel size reconstruction can be implemented for a cone beam-imaged optically absorbing, gelatin matrix-based gel dosimeter, given that the target position at the rear of the tank represents the lowest end of the spatial resolution range and most of the imaged volume still has an MTF value greater than 50% at 2 line pairs mm^{-1} .

3.3. Spatial distortion

In the evaluation of geometric distortion, negligible radial distortion was expected in the case where the refractive indices of the matching tank and jar media were well matched, but this was not the case. A small radial compression was observed (figure 8(c)), likely due to refractive index mismatch-derived distortion of light traveling through the dosimeter jar walls, and to a lesser extent, the matching tank windows. Further reduction in the radial compression can be achieved by lowering the refractive index of the tank media slightly below that of the jar media (typically by around 0.5%). Additional reduction in bath index beyond this point increases the spatial distortion.

Small day-to-day variations in index achieved after matching are not deemed to be of great importance to geometric distortion throughout most of the image volume, since the average radial compression for matched tank and jar media refractive index was reported to be $0.54 \pm 0.02\%$ for glycerol and $0.84 \pm 0.02\%$ for propylene glycol at room temperature. This corresponds to geometric distortions in the range of 0.2–0.3 mm, which have a minimal impact on dose spatial accuracy. The worst result at the third pin had a total radial compression of ~ 0.6 mm, which translates to only a single voxel shift, given that the reconstructed cubic voxel size is 0.5 mm. However, index mismatch can and does lead to problematic edge effects compromising the dosimetry near the container walls (for example, see the bottom two profiles in figure 11(b)). For this reason, regular attenuation should be given to bath-dosimeter index matching prior to imaging. On a final note, the results from this experiment are on par with previous results obtained using laser beam optical scanning system (Oldham and Kim 2004).

3.4. Scanner scatter measurement

The results in figure 9 indicate that the highest uncertainty region in the matching tank with and without the PETE jar was found to be at the top of the tank where there are reflections from the surface of the matching fluid solution or gelatin and the cone angle is great enough that there is reduced data coverage in the cone beam slice. In this situation of reduced

data coverage, limitations in reconstruction using the cone beam algorithm are observed (Smith 1985, Kak and Slaney 1998). The region near the bottom of the tank is similar to that at the top of the tank, except that it experiences less stray light perturbation (primarily reflections from the bottoms of the jar and matching tank) than the region near top of the tank, hence has a lower standard deviation. The observed noise and/or artifacts are generally reduced throughout the rest of the tank.

Localized exceptions to this are stray-light derived optical artifacts along the jar axis of rotation and near the jar wall edges (Babic *et al* 2009). Reflections off the band pass filter in front of the camera lens have previously been identified as one source of stray light artifacts and are reduced by tilting the band pass filter (Jordan and Battista 2006a). Overall, the results indicate that an 8 cm diameter, 10 cm high cylindrical ROI centered in the 1 L PETE jar volume image is the best-behaved (lowest measurement uncertainty) region for future work in 3D gel dosimetry. As the outer diameter of the PETE jar is 9.2 cm and the total imaged height of the PETE jar is 13 cm, this corresponds to $\sim 62\%$ of the total imaged volume of the jar. This ROI still incorporates the reduced (but measurable) reflection artifact at the center of the projection area. As long as this is understood, 3D dose in this perturbed region can be correctly interpreted.

The cone beam scanner exhibits low scatter attenuation measurement accuracy compared to the 'true' spectrophotometer measurement (figure 10(a)), a result that is primarily due to artifacts such as cupping in the data. As there are different effects that can give rise to cupping artifact (Al Nowais and Doran 2009), careful conclusions need to be drawn on the source of the cupping observed in figures 9(c) and 10(b). It is likely that scatter effects are the dominant source of cupping artifact over most of the useful measurement range of the scanner. However, wall effects are also a source of cupping. A few of the profiles in figure 10(b) show evidence of incomplete cancellation near the wall, which is a source of cupping in the data.

The difference in reconstructed attenuation between the two imaging wavelengths of 590 nm and 633 nm in figure 9(c) indicates that the attenuation falls somewhere between a third order and fourth order dependence on wavelength (i.e. close to the Rayleigh approximation). This indicates that scattering is the primary mechanism of attenuation in the gelatin matrix, and consequently, that angled scatter could be at least a partial, if not the dominant contributor to the observed cupping artifact, given the diffuse light source. The degree of cupping also increases with scatter solution concentration (figure 10(b)), which is consistent with this conclusion. Lastly, cupping has previously been observed when imaging scattering volumes using the Vista scanner (for example, see Bosi *et al* (2007, 2009)) and other optical CT scanners and effectively modeled as scatter perturbation (Oldham 2004, Bosi *et al* 2007, 2009). On this basis, it is safe to conclude that the major contributor to cupping artifact in cone beam optical CT imaging is angled scatter perturbation, and that this effect is the main source of the nonlinear attenuation behavior shown in figure 10(a). Since optically absorbing gel dosimeters incorporate a scattering gelatin or agarose matrix for spatial fixing of dose information, the extent to which the 'matrix scatter' source of uncertainty perturbs the data and limits of optical readout accuracy of absorbing gel dosimeters is critically important and will be addressed further in a later report addressing the management of stray light perturbation. The question of whether useful 3D dose information can be obtained from optically scattering dosimeters using the Vista scanner is also critical toward the 3D readout of polymer gels using a cone beam optical scanner. Experimental work has been completed in this regard, and results indicate that under tightly controlled conditions the cone beam optical CT readout of small field deliveries to scattering polymer gels is practically feasible. These results are outside the scope of this work, however, and will be reported at a later date.

3.5. Scanner absorption measurement

The near unity linear fit relationship between the 590 nm (RI 1.344) spectrophotometer and Vista scanner absorption measurements over the attenuation range of 0.0–0.2 cm⁻¹ in figure 11(a) gives good indication that the cone beam optical CT imaging provides accurate measurements of absorbing media. The fact that the slope of the data is approximately 3% below unity is mostly due to stray light perturbation, and to a lesser extent, spectral differences between the two imaging systems (Babic *et al* 2008). One indicator of stray light perturbation in the system is the bowing artifact (Jordan and Battista 2006a) seen in the reconstructed profiles of the absorbing solutions (figure 11(b)). This effect becomes more pronounced at higher absorption values. The management of, and correction for, this and other stray light effects in cone beam optical CT imaging is a significant topic in itself, and hence will be addressed more completely in a companion paper to this work. As a side note, a slight change in the bath index from 1.344 to 1.388 under 590 nm Vista scanner illumination did not introduce a significant change in the slope of the linear fit away from that obtained for the 590 nm (RI 1.344) spectrophotometer and Vista scanner absorption measurement data (figure 11(a)). This indicates that small day-to-day variations in refractive index due to evaporation of matching tank fluid are not likely a major determinant of scanner measurement precision and accuracy throughout most of the dosimeter volume, with localized exceptions near the dosimeter jar walls, as previously mentioned.

At mean jar attenuations greater than approximately 0.3 cm⁻¹, the relationship between Vista scanner and spectrophotometer absorption measurement significantly depart from linearity. For the 9.2 cm diameter scattering solution-filled 1 L PETE jar, this corresponds to a drop in transmission from reference to data scan through the center of the jar to approximately 10% of the full scale intensity in the CCD camera. This behavior is partly an effect of measurement at the lower end of the dynamic range of the camera, where pixel response to low light transmission becomes nonlinear (see figure 12(b)). A quick calculation using the results from figure 12(b) indicates that this effect could account for 10–20% of the difference between the spectrophotometer and cone beam optical CT measured values. The rest is likely due to stray light effects, the source of which will be discussed further in the previously mentioned companion paper to this work.

Longer shutter times could be employed to raise the recorded intensity into the CCD chip, in order to avoid the nonlinear behavior at the low end of the dynamic range. This is limited, however, by deleterious blooming effects from pixel saturation at the high end of the dynamic range (Krstajic and Doran 2007) in the regions outside the jar walls in the projection image. One way to extend the measurement range of the scanner to lower transmission values through the dosimeter (i.e. higher mean jar attenuation values) is to introduce absorbing dye into the matching tank fluid and increase camera shutter time and/or gain (Jordan and Battista 2009b). Another way is to employ a variable light field method described by Krstajic and Doran (2007).

Referring again to figure 10(a), it can be noted that there was no definitive upward or downward trend in measured attenuation over the 16 months' measurement trial period. It should also be noted that more than three scans were completed for some of the jar concentrations; the 0.05 g L⁻¹ and 0.10 g L⁻¹ solutions in particular were scanned several more times in other characterization work. The lack of trend in the results, therefore, suggest the possibility that the variation may at least in part be due to the scan conditions, which if better controlled would yield higher measurement precision. When close attention was given to scanner warm-up time, keeping the light source on throughout both scans, and using the optional Vista software projection normalization region, the measurement variation was

reduced to less than 1% inter-day precision for a 1.48 mg L^{-1} absorbing solution, as reported in table 1. The full investigation leading to the employment of these and other imaging protocols will be discussed more completely in a companion paper to this work.

Finally, the results presented in figure 12(a) indicate that a mean-to-standard deviation SNR of better than 100 is achieved in more than 60% of the jar volume image at attenuation values in the approximate range of $0.06\text{--}0.50 \text{ cm}^{-1}$ and $0.07\text{--}0.20 \text{ cm}^{-1}$ for absorbing and scattering media respectively at a 0.5 mm cubic voxel resolution. These data can then be combined with the accuracy results obtained from the Vista scanner–spectrophotometer comparison, indicating an approximate 3% accuracy for absorbing media mean jar attenuation values of $0.00\text{--}0.18 \text{ cm}^{-1}$. In this range, the standard deviation of the mean in-jar attenuation values was found to be on the order of 1.0–1.3%. Hence, an approximate 3–4% accuracy and the SNR of 100 or greater are obtained for more than 60% of the jar volume in 0.5 mm cubic voxel resolution reconstructed optical CT images over the absorption range of $0.06\text{--}0.18 \text{ cm}^{-1}$. The calibration scatter solution measurements, on the other hand, are nowhere near this level of accuracy over the entire range of measurement due to the observed nonlinear behavior arising from angled scatter stray light perturbation (figure 10(a)).

Extending these results into gel dosimetry, a Fricke–xylenol–gelatin (FXG)-filled 1 L PETE jar dosimeter, with an absorption contrast mechanism and a low scattering gelatin matrix attenuation (which should mostly cancel out as the baseline between the reference and data scans, to be discussed further in later work), should achieve approximately the same SNR of 100 and 3–4% measurement accuracy in 60+% of the imaged dosimeter volume for mean jar attenuation coefficients in the range of $0.06\text{--}0.18 \text{ cm}^{-1}$. The ‘dose resolution’ can then be calculated for a given FXG dosimeter sensitivity.

There are a few options available to improve the SNR at lower attenuation values. Multiple averages of each projection may possibly provide a slight improvement in the SNR, but come with the disadvantage of a longer scan time and will not remove the artifacts that mimic noise, such as refractive index mismatches, floating particles in the matching tank, scratches on the optics, etc. Post-acquisition filtering of projection (sinogram) data and reconstructed images also can improve the SNR without too great negative impact in lower dose gradient regions (Jirasek and Hiltz 2009), but can affect the measurement integrity at high dose gradients. Increased pre-reconstruction binning of the data in the Vista software may be another alternative. A higher pixel binning area does affect the 3D dose distribution at high dose gradients, but the tradeoff between the SNR and spatial integrity of dose may be managed carefully to ensure data integrity. At present, the preferred option is to keep the same imaging parameters and as high a resolution as possible (i.e. 0.5 mm cubic voxel size) and work toward further reduction of the other artifacts that mimic noise in the measurement. To maximize the SNR, careful attention to the dose sensitivity of the gel dosimeter is required to ensure that the post-irradiation attenuation values in the dosimeter jar are as high as possible to maximize SNR, but not so high that the transmitted intensity falls below approximately 10% of full scale intensity (i.e. into the nonlinear range of the detector) for any projection in the data scan.

4. Conclusions

With proper selection of camera lens aperture, the Vista cone beam CCD-based optical CT scanner conforms to the ‘narrow ray bundle’ condition of cone beam geometry for 3D imaging of optically absorbing dosimeters. The system was demonstrated to be capable of imaging both absorbing and scattering media to a reconstructed voxel resolution of $0.5 \times 0.5 \times 0.5 \text{ mm}^3$. At this resolution, a reconstructed optical CT image of a standard-sized 1 L PETE

jar dosimeter can be produced in less than 20 min total imaging and reconstruction time using a standard desktop computer. Although the absorption measurements show evidence of stray light perturbation, the scanner was shown to be capable of imaging more than 60% of the volume within an absorbing media-filled 1 L PETE jar dosimeter to a 0.5 mm cubic voxel resolution with minimal spatial distortion, an accuracy of 3–4% and the mean to standard deviation signal-to-noise ratio greater than 100 over an optical absorption range of 0.06–0.18 cm⁻¹. An inter-day scan precision of 1% was demonstrated for a representative absorbing media-filled 1 L PETE jar dosimeter with mean attenuation of 0.173 cm⁻¹ near the upper end of the preferred range of 0.06–0.18 cm⁻¹. The absorption measurements in this work are in reasonable agreement with the benchmark 1 × 1 × 1 mm³ spatial resolution, 60 min imaging time, 3% accuracy and 1% precision criteria suggested by Oldham *et al* (2001) for comparing optical CT to the ‘gold standard’ of MRI. This indicates that cone beam optical CT is a viable option for 3D readout of absorbing gel dosimeters. Future work addressing the effects of stray light perturbation should hopefully improve the accuracy and range of cone beam optical CT absorption measurement further. In contrast, the scanner has been observed to have much more limited capability in 3D imaging of optically scattering media. Consistent with previous investigations, artifacts arising from angled scatter and other forms of stray light perturbation have been shown to compromise the accuracy of attenuation measurement over the entire volume of the scattering media-filled 1 L PETE jar dosimeter. Additional calibration, stray light reduction, or stray light correction schemes will have to be explored in order to yield improved data from cone beam optical CT imaging of optically scattering dosimeters.

Acknowledgments

Research funding has been provided by the Canadian Institutes of Health Research and the Cancer Centre of Southeastern Ontario. The authors would like to thank Kevin Jordan from the London Regional Cancer Centre and Jen Dietrich and John Miller from Modus Medical Devices, Inc., for their helpful assistance.

References

- Al Nowais S and Doran S 2009 CCD-based optical CT scanning of highly attenuating phantoms *J. Phys.: Conf. Ser.* **164** 1–5
- Babic S, Battista J and Jordan K 2008 Three-dimensional dose verification for intensity-modulated radiation therapy in the radiological physics centre head-and-neck phantom using optical computed tomography scans of ferrous xylenol-orange gel dosimeters *Int. J. Radiat. Oncol. Biol. Phys.* **70** 1281–91
- Babic S, McNiven A, Battista J and Jordan K 2009 Three-dimensional dosimetry of small megavoltage radiation fields using radiochromic gels and optical CT scanning *Phys. Med. Biol.* **54** 2463–81
- Bayreder C, Schon R, Wieland M, Georg D, Moser E and Berg A 2008 The spatial resolution in dosimetry with normoxic polymer-gels investigated with the dose modulation transfer approach *Med. Phys.* **35** 1756–69
- Berg A, Pernkopf M, Waldhausl C, Schmidt W and Moser E 2004 High resolution MR based polymer dosimetry versus film densitometry: a systematic study based on the modulation transfer function approach *Phys. Med. Biol.* **49** 4087–108
- Bosi S, Naseri P, Puran A, Davies J and Baldock C 2007 Initial investigation of a novel light-scattering gel phantom for evaluation of optical CT scanners for radiotherapy gel dosimetry *Phys. Med. Biol.* **52** 2893–903
- Bosi S G, Brown S, Sarabipour S, De Deene Y and Baldock C 2009 Modelling optical scattering artefacts for varying pathlength in a gel dosimeter phantom *Phys. Med. Biol.* **54** 275–83
- DeJean P, Senden R J, McAuley K B, Rogers M and Schreiner L J 2006a Initial Experience with a commercial cone beam CT unit for polymer gel dosimetry: I. optical dosimetry issues *J. Phys.: Conf. Ser.* **56** 179–82
- DeJean P, Senden R J, McAuley K B, Rogers M and Schreiner L J 2006b Initial Experience with a commercial cone beam CT unit for polymer gel dosimetry: II. Clinical potential *J. Phys.: Conf. Ser.* **56** 183–6

- Doran S and Krstajic N 2006 The history and principles of optical computed tomography for scanning 3-D radiation dosimeters *J. Phys.: Conf. Ser.* **56** 45–57
- Doran S J, Koerkamp K K, Bero M A, Jenneson P, Morton E J and Gilboy W B 2001 A CCD-based optical CT scanner for high-resolution 3D imaging of radiation dose distributions: equipment specifications, optical simulations and preliminary results *Phys. Med. Biol.* **46** 3191–213
- Doran S J, Krstajic N, Adamovics J and Jenneson P M 2004 Optical CT scanning of PRESAGE(TM) polyurethane samples with a CCD-based readout system *J. Phys.: Conf. Ser.* **3** 240–3
- Feldkamp L A, Davis L C and Kress J W 1984 Practical cone-beam algorithm *J. Opt. Soc. Am.* **1** 612–9
- Gore J C, Kang Y S and Schulz R J 1984 Measurement of radiation dose distributions by nuclear magnetic resonance (NMR) imaging *Phys. Med. Biol.* **29** 1189–97
- Gore J C, Ranade M, Maryanski M J and Schulz R J 1996 Radiation dose distributions in three dimensions from tomographic optical density scanning of polymer gels: I. Development of an optical scanner *Phys. Med. Biol.* **41** 2695–704
- Guan H and Gordon R 1996 Computed tomography using algebraic reconstruction techniques (ARTs) with different projection access schemes: a comparison study under practical situations *Phys. Med. Biol.* **41** 1727–43
- Hillier J 1949 Some remarks on the image contrast in electron microscopy and the two-component objective *J. Bacteriol.* **57** 313–7
- Islam K T, Dempsey J F, Ranade M K, Maryanski M J and Low D A 2003 Initial evaluation of commercial optical CT-based 3D gel dosimeter *Med. Phys.* **30** 2159–68
- Jirasek A and Hilts M 2009 An overview of polymer gel dosimetry using x-ray CT *J. Phys.: Conf. Ser.* **164** 246–56
- Jordan K and Battista J 2006a Linearity and image uniformity of the VistaTM optical CT scanner *J. Phys.: Conf. Ser.* **56** 217–20
- Jordan K and Battista J 2006b Small, medium and large optical cone beam CT *J. Phys.: Conf. Ser.* **56** 214–6
- Jordan K and Battista J 2009a Scatter measurements for optical cone-beam computed tomography *J. Phys.: Conf. Ser.* **164** 159–63
- Jordan K and Battista J R 2009b A stable black-refractive-index-matching liquid for optical CT scanning of hydrogels *J. Phys.: Conf. Ser.* **164** 290–3
- Kak A C and Slaney M 1998 *Principles of Computerized Tomographic Imaging* (Philadelphia, PA: Society for Industrial and Applied Mathematics) p 104–7
- Kelly B G, Jordan K J and Battista J J 1998 Optical CT reconstruction of 3D dose distributions using the ferrous-benzoic-xyleneol (FBX) gel dosimeter *Med. Phys.* **25** 1741–50
- Krstajic N and Doran S J 2006 Focusing optics of a parallel beam CCD optical tomography apparatus for 3D radiation gel dosimetry *Phys. Med. Biol.* **51** 2055–75
- Krstajic N and Doran S J 2007 Characterization of a parallel-beam CCD optical-CT apparatus for 3D radiation dosimetry *Phys. Med. Biol.* **52** 3693–713
- Lopatiuk-Tirpak O, Langen K M, Meeks S L, Kupelian P A, Zeidan O A and Maryanski M J 2008 Performance evaluation of an improved optical computed tomography polymer gel dosimeter system for 3D dose verification of static and dynamic phantom deliveries *Med. Phys.* **35** 3847–59
- Marks D L, Stack R, Johnson A J, Brady D J and Munson D C 2001 Cone-beam tomography with a digital camera *Appl. Opt.* **40** 1795–805
- Maryanski M J, Gore J C, Kennan R P and Schulz R J 1993 NMR relaxation enhancement in gels polymerized and cross-linked by ionizing radiation: a new approach to 3D dosimetry by MRI *Magn. Reson. Imaging* **11** 253–8
- Maryanski M J, Zastavker Y Z and Gore J C 1996 Radiation dose distributions in three dimensions from tomographic optical density scanning of polymer gels: II. Optical properties of the BANG polymer gel *Phys. Med. Biol.* **41** 2705–17
- Oldham M 2004 Optical-CT scanning of polymer gels *J. Phys.: Conf. Ser.* **3** 122–35
- Oldham M and Kim L 2004 Optical-CT gel-dosimetry: II. Optical artifacts and geometrical distortion *Med. Phys.* **31** 1093–104
- Oldham M, Siewerdsen J H, Kumar S, Wong J and Jaffray D A 2003 Optical-CT gel-dosimetry: I. Basic investigations *Med. Phys.* **30** 623–34
- Oldham M, Siewerdsen J H, Shetty A and Jaffray D A 2001 High resolution gel-dosimetry by optical-CT and MR scanning *Med. Phys.* **28** 1436–45
- Olding T, Holmes O and Schreiner L J 2009 Scatter corrections for cone beam optical CT *J. Phys.: Conf. Ser.* **164** 174–8
- Olsson L E, Fransson A, Ericsson A and Mattsson S 1990 MR imaging of absorbed dose distributions for radiotherapy using ferrous sulphate gels *Phys. Med. Biol.* **35** 1623–31

- Olsson L E, Westrin B, Fransson A and Nordell B 1992 Diffusion of ferric ions in agarose dosimeter gels *Phys. Med. Biol.* **37** 2243–51
- Robb R A 1982 The dynamic spatial reconstructor: an x-ray video-fluoroscopic CT scanner for dynamic volume imaging of moving organs *IEEE Trans. Med. Imaging* **1** 22–33
- Schreiner L J 2009 Where does gel dosimetry fit in the clinic? *J. Phys.: Conf. Ser.* **164** 1–12
- Schreiner L J and Olding T 2009 Gel dosimetry *AAPM Medical Physics Monograph No. 34: Clinical Dosimetry Measurements in Radiotherapy* ed D W Rogers and J E Cygler (Madison, WI: Medical Physics Publishing)
- Smith B D 1985 Image reconstruction from cone-beam projections: necessary and sufficient conditions and reconstruction methods *IEEE Trans. Med. Imaging* **4** 14–25
- Tarte B J and van Doorn T 1993 Optical scanning of ferrous sulphate gels for radiotherapy treatment dosimetry *APSEM/BECON Australasian Conf. on Physical Science and Engineering in Medicine/Biomedical Engineering*
- Tarte B J and van Doorn T 1995 Laser based tomographic scanning of gel volumes for applications in ionising radiation dosimetry *10th Conf. of the Australasian Optical Society (University of Queensland)*
- van Doorn T, Bhat M, Rutten T P, Tran T and Costanzo A 2005 A fast, high spatial resolution optical tomographic scanner for measurement of absorption in gel dosimetry *Australas. Phys. Eng. Sci. Med.* **28** 76–85
- Wolodzko J G, Marsden C and Appleby A 1999 CCD imaging for optical tomography of gel radiation dosimeters *Med. Phys.* **26** 2508–13